Surface defect-engineered CeO_{2-x} by ultrasound
treatment for superior photocatalytic H_2 production
and water treatment

Ultrasound vibrations towards ceria nanoparticles
disseminated the active elements and engineered oxygen
vacancies on its surface in conjunction with more significant
active sites. This approach excelled the photocatalytic
hydrogen production with a quantum efficiency of 1.125%
and the photocatalytic wastewater mineralization.

As featured in:

ROYAL SOCIETY
OF CHEMISTRY

rsc.li/catalysis

Catalysis Science & Technology

PAPER

Check for updates

Surface defect-engineered CeO$_{2-x}$ by ultrasound treatment for superior photocatalytic H$_2$ production and water treatment†

Sujay Shekar G. C., [iD] [a] Khaled Alkanad, [a] Gubran Alnaggar, [iD] [b] Nabil Al-Zaqri, [iD] [c] Mohammed Abdullah Bajiri, [iD] [d] Thejaswini B., [e] M. D. Dhileepan, [f] Bernaurdshaw Neppolian [iD] [f] and Lokanath N. K. [iD] *[a]

Semiconductor photocatalysts with surface defects display incredible light absorption bandwidth and these defects function as highly active sites for oxidation processes by interacting with the surface band structure. Accordingly, engineering the photocatalyst with surface oxygen vacancies will enhance the semiconductor nanostructure's photocatalytic efficiency. Herein, a CeO$_{2-x}$ nanostructure is designed under the influence of low-frequency ultrasonic waves to create surface oxygen vacancies. This approach enhances the photocatalytic efficiency compared to many heterostructures while keeping the intrinsic crystal structure intact. Ultrasonic waves induce the acoustic cavitation effect leading to the dissemination of active elements on the surface, which results in vacancy formation in conjunction with larger surface area and smaller particle size. The structural analysis of CeO$_{2-x}$ revealed higher crystallinity, as well as morphological optimization and the presence of oxygen vacancies is verified through Raman, X-ray photoelectron spectroscopy, temperature-programmed reduction, photoluminescence, and electron spin resonance analyses. Oxygen vacancies accelerate the redox cycle between Ce^{4+} and Ce^{3+} by prolonging photogenerated charge recombination. The ultrasound-treated pristine CeO$_2$ sample achieved excellent hydrogen production showing a quantum efficiency of 1.125% and efficient organic degradation. Our promising findings demonstrated that ultrasonic treatment causes the formation of surface oxygen vacancies and improves photocatalytic hydrogen evolution and pollution degradation.

1. Introduction

It is widely believed that using a solar source for energy production and pollution removal is the most effective technique for the world's energy problem and environmental deprivation. Tremendous efforts have been put into turning solar energy into a usable energy medium through photocatalysis, which emerged as the most favourable photoconversion technique as it uses sunlight to reduce environmental pollution and produce solar fuels like hydrogen, methanol, and so on.[1] H$_2$ is used as a fuel for automobiles and helps to tackle the challenges of greenhouse effect and ecological sustainability.[2] The production of H$_2$ through oxidation of hydrocarbons or reforming of natural gas takes enormous amount of energy and more expensive. Nevertheless, photocatalytic H$_2$ evolution is a green, recyclable and cost-effective technique for production of carbon-free fuel.[3] On the other hand, many hazardous contaminants are disposed into the water sources due to the rapid expansion of textile, pharmacological and food industries causing immense water pollution. Industrial pollutants like rhodamine B, brilliant blue, methyl orange dyes and phenol derivatives represent the major group of organic compounds responsible for water contamination which makes photocatalysis a great prospective candidate in water treatment.[4]

Semiconductor nanostructures have demonstrated promising progress in the development of photocatalysis. Whilst pristine semiconductors have a broad light-absorption range, they are frequently plagued by severe electron–hole

[a] *Department of Studies in Physics, University of Mysore, Manasagangotri, Mysuru 570006, India. E-mail: lokanath@physics.uni-mysore.ac.in*

[b] *Department of Studies in Chemistry, University of Mysore, Manasagangotri, Mysuru 570006, India*

[c] *Department of Chemistry, College of Science, King Saud University, Riyadh 11451, Saudi Arabia*

[d] *Department of Studies and Research in Industrial Chemistry, School of Chemical Sciences, Kuvempu University, Shankaraghatta 577451, India*

[e] *PG Department of Physics, St. Philomena's College, University of Mysore, Bannimantap, Mysore 570015, India*

[f] *Energy and Environmental Remediation Lab, SRM-Research Institute of Science and Technology, Chennai 603203, India*

† Electronic supplementary information (ESI) available. See DOI: 10.1039/d1cy01940f

This journal is © The Royal Society of Chemistry 2022

Catal. Sci. Technol., 2022, **12**, 2071–2083 | **2071**

recombination and poor adsorption on their surfaces.[5] Consequently, the efficiency of charge kinetics operations is greatly reduced, and the photocatalytic activity is significantly decreased. Several techniques have been studied to enhance the photocatalytic efficiency of semiconductor nanostructures like defect engineering, doping of metals or non-metals, construction of heterojunctions, metal loading, *etc.*,[6–8]

Engineering defects in semiconductor photocatalysts is an efficient method to control and change the regional coordination of active sites in semiconductor photocatalysts.[9] For altering the bandgap energies in nanostructures and improving photoexcited electron transport, defect engineering offers great potential.[10] Using bulk defects in semiconductors, light absorption bandwidth may be broadened by modulating the band structure, while surface defects can act as highly active sites for oxidation processes by interacting with the surface band structure.[11] The development of zero-dimensional point defects such as vacancy generation with various atomic structures in pristine nanostructures can regulate the non-stoichiometric composition of photocatalysts without the need for the introduction of co-catalysts.[12] Thus, it is crucial to design photocatalysts with surface defects to increase the efficiency of pristine semiconductor nanostructures.

Ceria, the most abundant rare-earth element, offers many desirable properties as a typical n-type semiconductor, including nontoxicity and sensitivity to photoirradiation.[13] The widespread use of ceria as a catalyst for oxidation catalysis is owing to its remarkable oxygen storage capacity, which is a result of its exceptional redox characteristics, which makes it an excellent choice for photocatalytic application.[14] The photocatalytic efficiency is enhanced by appropriately utilizing these properties and keeping the intrinsic crystal structure intact compared to many heterostructures.[7,15] The higher Ce^{3+} concentration and subsequent oxygen vacancy formation in CeO_2 are valuable in enhancing the photocatalytic efficiency.[16] These oxygen vacancies have the potential to prolong the lifespan of charge carriers and therefore contribute to the creation of free electrons and holes, resulting in more active species serving in organic degradation. Consequently, the OH stability through the surface oxygen vacancies supports the pathway for higher hydrogen production.[17]

Researchers have synthesized ceria nanostructures with surface oxygen vacancies under different methods. Bui *et al.* found that base treatment for CeO_2 nanostructures exhibited more oxygen vacancies on the surface.[5] Wang *et al.* reported that CeO_{2-x} showed increased oxygen vacancy concentration with the help of Cu doping to promote photocatalytic activities.[6] Hezam *et al.* reported a sunlight-driven synthesis method to fabricate CeO_2 nanostructures with oxygen vacancies which was assisted by the use of dense convex lens.[7] Choudhury *et al.* found a way through hydrolysis to red shift the band gap with the presence of surface defects for CeO_2 nanoparticles.[18] Zhang *et al.* showed that the self-doping of Ce^{3+} in CeO_2 will promote the formation of

oxygen vacancies.[19] These synthesis methods to generate oxygen vacancies were aided with expensive instrumentations, doping of metals and various complex chemical processes leading to many drawbacks like thermal instability, dopant concentration dependency, short-term efficiency, adsorption by other coexisting species, tedious multi-step experimental procedures and average photocatalytic activity.[20–22]

The ultrasound-assisted approach for synthesizing photocatalysts is cost-effective and exhibits more capability than the conventional techniques which could regulate the surface defects without any dependency and displayed notable reusability. The cavitation phenomena caused by the ultrasonic waves show telekinetic effects on the surface of the photocatalyst by accelerating the dissemination of active elements.[23] This fascinating cavitation effect corresponding to local high pressure and temperature, intense shear stress, and strong acoustic streaming is caused by the implosion of cavitation bubbles and turbulence resulting in breaking of the bonds allowing the reaction to occur more rapidly.[24,25] Moreover, the amount of energy created by the ultrasonic reaction generates charge carriers (electron–hole pairs). A generated hole interacts with a Ce–O bond binding electron. As a consequence of the bond breaking, the single oxygen atom on the surface of CeO_2 desorbs as oxygen (upon coupling with the other O atom), forming an oxygen vacancy. In the meantime, certain Ce^{4+} ions capture electrons and get converted to Ce^{3+}. Besides, the ultrasound treatment enhances the specific area of nanostructures with active sites resulting in higher photocatalytic efficiency.[26]

In this work, CeO_2 is defect-engineered to obtain surface oxygen vacancies by employing ultrasonic irradiation and used for enhanced photocatalytic hydrogen production and photocatalytic degradation of brilliant blue and phenol. The CeO_{2-x} nanostructure is designed under the influence of low-frequency ultrasonic waves for the first time to produce surface defects. The formation of oxygen vacancies is confirmed by a variety of sophisticated analytical methods. The effect of ultrasound and the significant role of surface oxygen vacancies in higher hydrogen production is studied through the reaction pathway.

2. Materials and methods

2.1. Precursors

Chemical reagents like cerium(III) nitrate hexahydrate [$Ce(NO_3)_3 \cdot 6H_2O$], glycine [$C_2H_5NO_2$], sodium hydroxide [$NaOH$], nitric acid [HNO_3], triethanolamine, brilliant blue [$C_{37}H_{34}N_2Na_2O_9S_3$] and phenol [$C_6H_5OH$] were purchased from Sigma Aldrich. All the chemicals were of pure analytical grade and were used without any further purification. Deionized water was used for all the experiments.

2.2. Preparation of the catalyst

The CeO_2 photocatalyst was prepared by a solution combustion method. In a 200 mL beaker, 0.15 M

2072 | *Catal. Sci. Technol.*, 2022, **12**, 2071–2083

This journal is © The Royal Society of Chemistry 2022

$Ce(NO_3)_3 \cdot 6H_2O$ was added with an appropriate amount of glycine as a fuel in 20 mL deionized water in such a way that the fuel ratio was equal to 1. The mixture was vigorously stirred at room temperature for 45 min and heated at 300 °C. Initially, the solution starts boiling, then later turns to foam, and finally gets ignited and burnt. The formed powder was kept in a muffle furnace at 500 °C for 1 h to form CeO_2 nanoparticles.

2 g of the prepared CeO_2 was dispersed in 100 mL of ethanol and stirred vigorously at room temperature. The solution was kept in an ultrasonic bath operating at 20 kHz with 100 W power containing water for stabilizing the temperature. The solution is then exposed to ultrasound irradiation for 3 h. The precipitate is later purified by filtration and washed with distilled water three times. Finally, the product was dried in a hot-air oven for 90 °C for 12 h to obtain CeO_{2-x} nanoparticles.

2.3. Optical and analytical studies

Powder X-ray diffraction (XRD) was carried out using a Rigaku X-ray diffractometer (Cu Kα radiation, λ = 1.54059 Å) to detect crystal patterns. The morphology of the fabricated products was analyzed using a scanning electron microscope (SEM, Hitachi-3400 N) and a high-resolution transmission electron microscope (TEM, Tecnai G2, F30). Fourier transform infrared analysis (FTIR) was carried out using a JASCO 460 plus FTIR spectrometer. Laser Raman spectrometer (Horiba, Xplora plus) was used to record the Raman spectra. Elemental analysis was carried out by energy dispersive X-ray analysis (EDAX) and X-ray photoelectron spectroscopy (XPS, PHI 5000 Versa Probe III). Hydrogen temperature-programmed reduction (H_2-TPR) was carried out on a Micromeritics Autochem 2920 equipped with a thermal conductivity detector. Particle size distribution was investigated using dynamic light scattering (DLS, Microtrac W3231). The specific surface area of the synthesized materials was measured using a Brunauer–Emmett–Teller analyzer (Belsorp mini-2). The bandgap of the material was determined using UV-visible diffuse reflectance spectroscopy (DRS UV-vis). Photoluminescence (PL) spectra of the sample were recorded using a Shimadzu RF-6000 fluorescence spectrophotometer. Liquid chromatography mass spectroscopy (LCMS) was carried out to identify the intermediate products utilizing an Agilent G6545B, USA. Total organic carbon (TOC) was measured using an Analytik Jena multi N/C 3100 analyzer.

2.4. Photocatalytic assessment

The photocatalytic hydrogen production was carried out under a xenon lamp having a power of 300 W with a 420 nm cutoff filter and light intensity around 100 mW cm^{-2}. The process was carried out inside a quartz reactor by dispersing 5 mg of the sample in 50 ml of the aqueous solution containing triethanolamine (TEOA) as a sacrificial agent. The system was kept under continuous magnetic stirring at the rate of 300 rpm, and a temperature around 27 °C was maintained during the experiment. The suspension was later purged with nitrogen to eliminate the dissolved oxygen, maintaining anaerobic conditions for 30 min. After irradiating the suspension, the amount of hydrogen produced was analyzed periodically using an off-line Shimadzu GC-2014 gas chromatograph equipped with a thermal conductivity detector.

The photocatalytic activity of the materials was also studied by the degradation of brilliant blue dye (BB) under visible light irradiation. In a typical method, the catalyst (0.5 g L^{-1}) and the BB (10 mg L^{-1}) solution mixture are stirred in the dark for 30 min to accomplish adsorption–desorption equilibrium before sunlight irradiation. The absorption band of BB is detected at an equal interval of time using a UV-vis spectrophotometer to verify the productivity of the catalyst.

Additionally, the photocatalytic efficiency of the prepared samples was examined by the degradation of phenol. The suspension containing 200 ml of phenol (30 mg L^{-1}) and 0.1 g of the photocatalyst was stirred at room temperature until it reached equilibrium. After visible light irradiation, 5 ml aliquots were collected from the suspension at an equal time interval. The phenol concentration was tested using the 4-aminoantipyrine spectrophotometric method.

2.5. Electrochemical studies

The measurements of photocurrent and electrochemical impedance were carried out using a CHI 608e electrochemical workstation. The sample was mixed appropriately with isopropanol and Nafion solution to spin-coat on fluorine-doped tin oxide glass, forming the working electrode. At the same time, a platinum wire and Ag/AgCl electrode were respectively used as counter and reference electrodes. The standard three-electrodes were immersed in an aqueous solution containing 0.5 M Na_2SO_4 as the electrolyte. Solar simulation with a 100 mW cm^{-2} intensity from a 250 W Xe lamp was conducted to irradiate the working electrode, and the photoresponse was measured at 0 V during the light on–off cycle. The electrochemical impedance was assessed under the same setup under open circuit conditions in a frequency range of 1 to 0.1 MHz with an AC voltage of 5 mV amplitude.

2.6. Electron spin resonance analysis

The electron spin resonance (ESR) signals were recorded using a Bruker EMXplus ESR spectrometer at 9.64 GHz microwave frequency and 1 mW power at room temperature. The sample was precipitated suitably in an aqueous solution containing 15 mM 5,5-dimethyl pyrroline N-oxide (DMPO). $\cdot O_2^-$ and $\cdot OH$ were detected using methanol and aqueous solution of DMPO, respectively. For the detection of $^1O_2$, the sample was precipitated in an aqueous solution containing 2,2,6,6-tetramethypiperidine (TEMP). The suspension was irradiated for 20 min by a 250 W Xe lamp
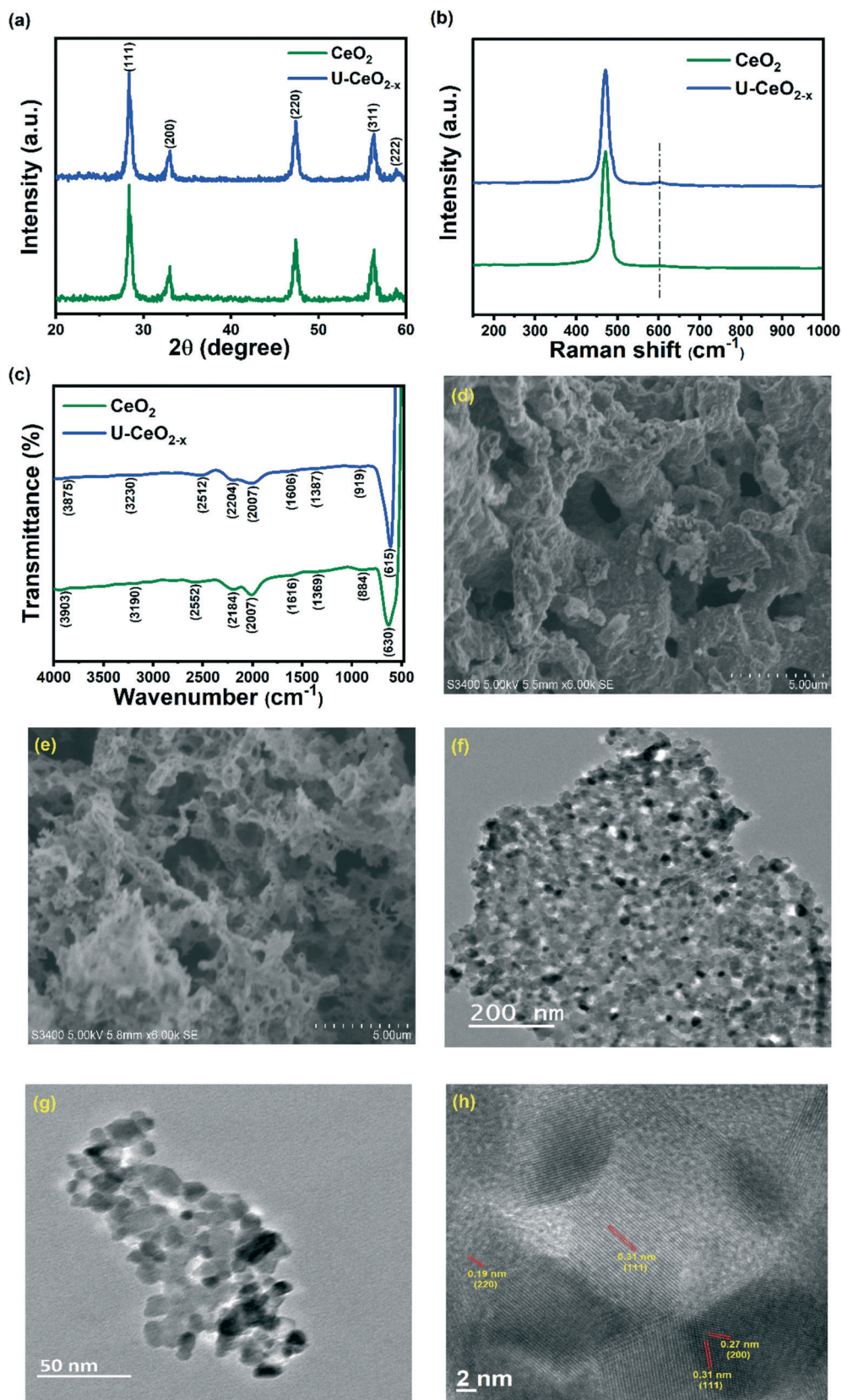
Fig. 1 (a) Powder X-ray diffraction patterns, (b) Raman spectra, and (c) FTIR spectra of the synthesized samples. SEM images of (d) CeO_2 and (e) U-CeO_{2-x}. (f and g) TEM images and (h) HRTEM image of the U-CeO_{2-x} sample.

2074 | *Catal. Sci. Technol.*, 2022, **12**, 2071–2083

This journal is © The Royal Society of Chemistry 2022

having a light intensity of 100 mW cm^{-2}, and the signals were recorded at room temperature.

3. Results and discussion

3.1. Characterization of the catalysts

The X-ray diffraction patterns of the synthesized CeO$_2$ and ultrasound-treated CeO$_{2-x}$ (U-CeO$_{2-x}$) are compared as shown in Fig. 1a. The diffraction peaks in both XRD patterns follow the cubic fluorite phase of CeO$_2$ and appear at 28.4, 33, 47.4, 56.3, and 58.9°, which are indexed to (111), (200), (220), (311), and (222), respectively (JCPDS card no. 75-0076).[7]

The Raman spectra of CeO$_2$ and U-CeO$_{2-x}$ are displayed in Fig. 1b. The standard peak of CeO$_2$ positioned at 470.6 cm^{-1} is ascribed to the F$_{2g}$ mode of a fluorite-type structure.[27] Meanwhile, the presence of oxygen vacancies is demonstrated by a minor peak at 602 cm^{-1}.[28] The minor shift and the presence of Ce^{3+} in U-CeO$_{2-x}$ have confirmed the intrinsic oxygen vacancies.

The synthesized CeO$_2$ and U-CeO$_{2-x}$ samples were subjected to FTIR analysis. Fig. 1c shows the FTIR spectra of the synthesized samples recorded in the range of 400–4000 cm^{-1}. The intense peak at 630 cm^{-1} is assigned to Ce–O–Ce stretching vibration, confirming the formation of CeO$_2$.[29] The C=O and C–O bond vibrations are observed at around 884 and 1369 cm^{-1}, respectively. The band at 1616 cm^{-1}

corresponds to the bending vibration of H$_2$O absorbed from the atmosphere. The bands observed at 2007 and 2184 cm^{-1} are ascribed to the stretching vibration of C–H bonds. The small band at 2552 cm^{-1} is due to the absorption of atmospheric CO$_2$. The weak bands at 3190 and 3903 cm^{-1} are attributed to the OH stretching of water.[30]

The morphology of the synthesized samples was investigated through SEM and TEM analysis. Fig. 1(d) shows the CeO$_2$ nanoparticles having a porous network-like structure, and Fig. 1(e) shows U-CeO$_{2-x}$ having a spongy network-like structure with larger pores than its counterpart, indicating a smaller size of the particles. Fig. 1(f and g) show the TEM images of the U-CeO$_{2-x}$ sample demonstrating a uniform particle distribution with a smaller size. The HRTEM image shown in Fig. 1(h) shows the lattice fringes of the CeO$_{2-x}$ sample with 0.31 nm, 0.27 nm and 0.19 nm interlayer spacings for the (111), (200) and (220) planes, respectively, with better interplanar interface contact. This result is in agreement with the XRD studies.

EDAX with SEM was carried out to confirm the purity of the samples further. The EDAX spectrum shown in Fig. S1† confirms the Ce, O, and C elements in the photocatalyst. The weight percentages of Ce, O, and C were around 66.97, 28.94, and 4.09%, respectively.

The oxidation states and the presence of oxygen vacancies are determined by XPS analysis. The XPS spectrum of CeO$_2$
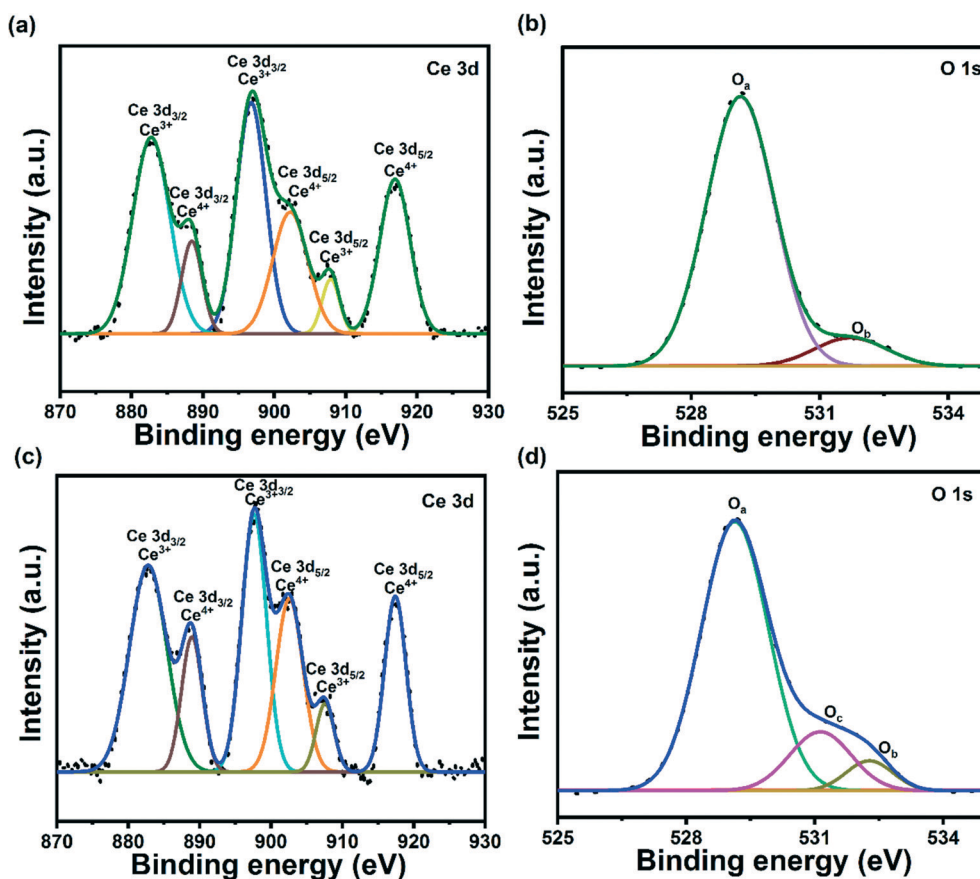

Fig. 2   Ce 3d XPS spectrum of (a) CeO$_2$ and (c) U-CeO$_{2-x}$. O 1s XPS spectrum of (b) CeO$_2$ and (d) U-CeO$_{2-x}$.

and U-CeO$_{2-x}$ is shown in Fig. 2(a–d). The Ce 3d split levels are deconvoluted and fitted to analyze additional peaks and intensity variation. The peaks due to the Ce 3d$_{3/2}$ level for Ce^{3+} ions are found at 882.7 and 896.9 eV, whereas, for the Ce^{4+} state, a peak at 888.1 eV is formed.[31,32] At the same time, the peak owing to the Ce 3d$_{5/2}$ level for Ce^{4+} cations has appeared at 902 and 916.9 eV along with a peak at 907.6 eV for the Ce^{3+} state.[7,28,33] The observed peaks for the U-CeO$_{2-x}$ sample have the same peaks with a minor variation in their positions; nevertheless, a noteworthy change in the intensity of the peaks was observed. The ultrasound irradiation has affected CeO$_2$ with a better proportion of Ce^{3+} ions [59.54%], which ultimately demonstrates as a critical factor for the formation of oxygen vacancies and improved catalytic activity.[34] The signature of oxygen vacancies is ultimately traced in the XPS profile of O 1s. The conventional

combustion-synthesized CeO$_2$ showed characteristic peaks of lattice oxygen (O$_a$) and surface OH$^-$ (O$_b$) at 529.14 and 531.9 eV, respectively.[35,36] On the other hand, the ultrasound-treated CeO$_2$ along with the characteristic peaks exhibited an elevated peak corresponding to chemisorbed oxygen (O$_c$) at 531.2 eV.[7] The chemisorbed oxygen indicates the presence of oxygen vacancies and enhances the mobility over the catalyst.[28,37,38] Thus, a larger proportion of chemisorbed oxygen species [15.64%] and the significant Ce^{3+} ions indicate the evolution of higher oxygen vacancies. Due to the oxygen vacancies, free electrons and holes are created resulting in more active species for enhanced degradation of contaminants. Accordingly, the hydrogen evolution has been boosted due to the stability of OH caused by surface oxygen vacancies. These results are shown in Table S1.† The relative portions of Ce^{3+} and oxygen vacancies are calculated using the formulas:
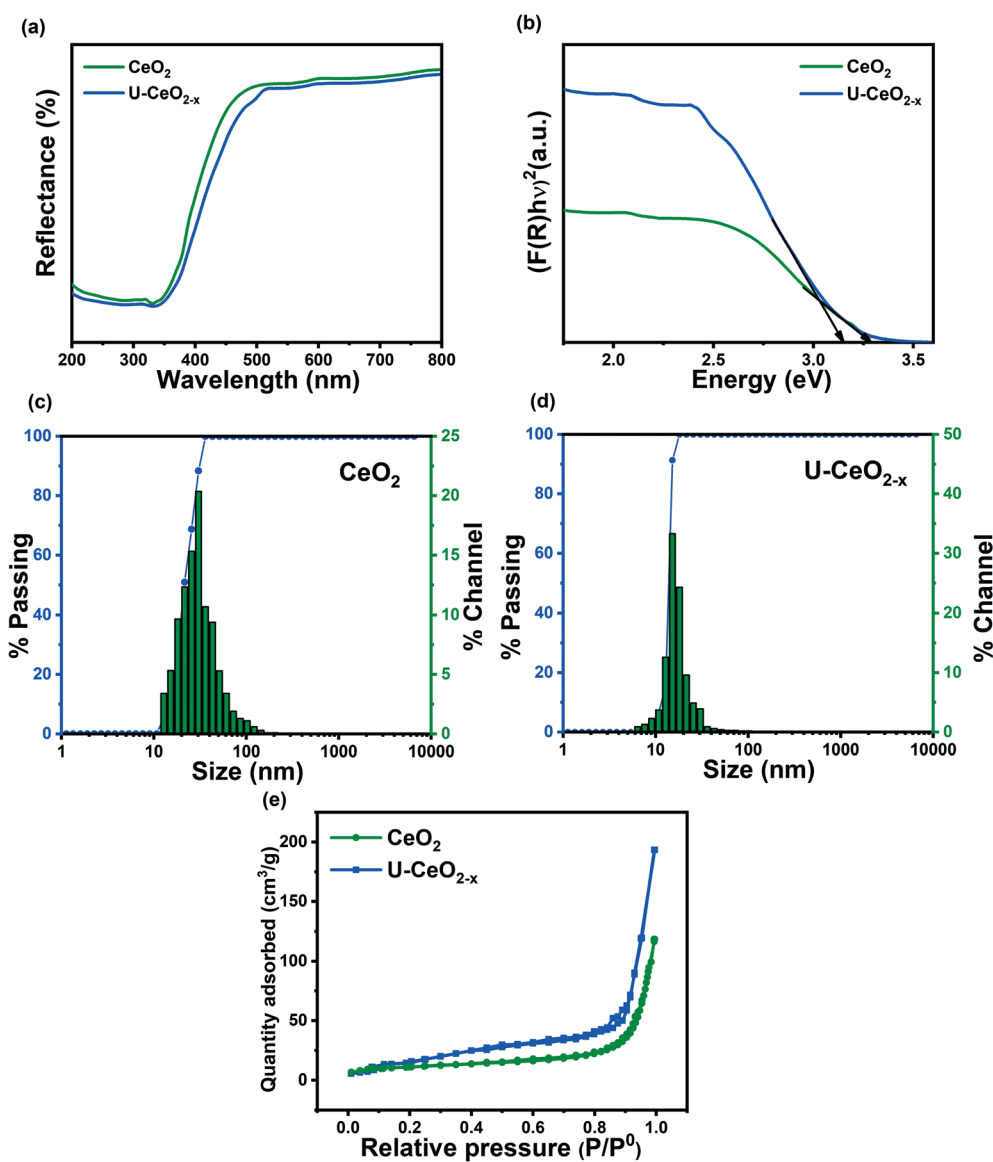

Fig. 3 (a) UV-vis reflectance spectra and (b) bandgap energy estimation using the Kubelka–Munk function for the synthesized samples; DLS spectra of the (c) CeO$_2$ and (d) U-CeO$_{2-x}$ samples; (e) nitrogen adsorption and desorption isotherms of the samples.

2076 | *Catal. Sci. Technol.*, 2022, **12**, 2071–2083

This journal is © The Royal Society of Chemistry 2022

$$C[Ce^{3+}]\% = \frac{Ce^{3+}}{(Ce^{3+} + Ce^{4+})} \times 100$$

$$C[O_c]\% = \frac{O_c}{(O_a + O_b + O_c)} \times 100$$

The presence of defects on the surface is further verified through H_2-temperature programmed reduction (H_2-TPR) analysis. A H_2 consumption rate was obtained for both the samples (see Fig. S2†) and CeO_{2-x} showed a higher H_2 consumption amount due to higher oxygen on the surface. The presence of the peak around 395 °C in the U-CeO_{2-x} sample corresponds to active oxygen, suggesting more Ce^{3+} and surface oxygen vacancies.[39]

An optical reflectance study to measure the bandgap was carried out using DRS analysis. Fig. 3a shows the UV-vis DRS spectra of the CeO_2 and U-CeO_{2-x} samples. The ultrasound-treated sample showed a relatively lower reflectance rate indicating higher absorption of the corresponding wavelength. Since U-CeO_{2-x} exhibits better absorption of UV and visible wavelength, it demonstrates an enhanced photocatalytic activity. From the spectra, the Kubelka–Munk function for measuring the bandgap can be used as,[40]

$$F(R_\infty) = \frac{K}{S} = \frac{(1 - R_\infty)^2}{2R_\infty}$$

$$F(R_\infty)h\nu = A(h\nu - E_g)^n$$

where R_∞ is the reflectance with an infinite thickness for the sample, A indicates the proportionality constant, h denotes the Plank's constant, ν is the frequency of the light, E_g represents the bandgap, and K and S are the absorption and scattering coefficients, respectively. The direct bandgap measured using the Kubelka–Munk function from the spectra was around 3.28 and 3.14 eV for CeO_2 and U-CeO_{2-x}, respectively, as shown in Fig. 3b. The bandgap excitation of electrons from O (2p) to the Ce (4f) levels is the principle transition of CeO_2.[41] The UV photons perhaps cause the 4f transitions and formation of the Ce^{3+} phase, eventually enhancing photocatalytic activity.[42]

The particle size distribution was analyzed by performing DLS for the samples, as shown in Fig. 3(c and d). The catalyst's aggregate size impacts the kinetics of photocatalytic activity since the smaller particle size exhibits a higher surface area leading to better photocatalytic performance.[43,44] The CeO_2 sample shows a size distinction of around 33.9 nm, while the U-CeO_{2-x} sample displayed a particle diameter of about 15.6 nm. This infers that U-CeO_{2-x} has ample surface defects exhibiting enhanced photocatalytic efficiency.

The surface area of the prepared samples was examined using a Brunauer–Emmett–Teller (BET) surface analyzer, as shown in Fig. 3e. The nitrogen absorption–desorption isotherm showed an H3-type hysteresis loop with a type III isotherm signifying a mesoporous structure.[45] The specific surface area of U-CeO_{2-x} (51.3 m^2 g^{-1}) was comparatively higher than that of the CeO_2 (19.8 m^2 g^{-1}) sample. Thus, the high surface area and mesoporosity of U-CeO_{2-x} have resulted in a higher probability of surface reaction and improved photocatalytic activity.

3.2. Photocatalytic activity and mechanism.

The photocatalytic activity of the prepared samples was investigated by the rates of hydrogen production and degradation tests with BB dye and phenol under visible light irradiation. Fig. 4a shows the hydrogen production rate for the CeO_2 and U-CeO_{2-x} samples. A substantial quantity of H_2 was produced by the U-CeO_{2-x} nanostructure, favored by the presence of oxygen vacancies. It is observed that the photocatalytic H_2 production by the U-CeO_{2-x} nanostructure was 2570 µmol h^{-1} g^{-1}, which is 2.7 times higher productivity than the CeO_2 nanostructure (950 µmol h^{-1} g^{-1}), and the proportional increase in the production rate confirms the photostability of the sample. This enhanced photocatalytic activity can be ascribed to the increased light absorption and effective charge recombination rate. The reproducibility of the U-CeO_{2-x} sample was verified under similar conditions for 2 h, where the sample is removed by filtering and washed with distilled water, and then dried and reused for the next cycle. Fig. 4b shows the reproducibility effects and confirms the structural stability of the sample. The quantum efficiency is measured as,[46]

$$Quantum\ efficiency = \frac{number\ of\ H_2\ molecules\ evolved \times 2}{number\ of\ incident\ photons}$$

The apparent quantum efficiency of the U-CeO_{2-x} sample is 1.125%, much higher than those of any other pure CeO_2 and many other CeO_2-based composites synthesized under various methods. The hydrogen production performance is compared with previous literature as shown in Table 1.

The photocatalytic degradation test is conducted with BB dye and phenol under visible light. Fig. 4c and d show the BB and phenol degradation curves of the U-CeO_{2-x} sample at 595 nm and 270 nm, respectively, for different irradiation times. The adsorption activity was assessed under dark conditions for both dye and phenol, where the results are displayed in Fig. 4e and f, respectively. The photocatalytic competence of the samples was calculated,

$$\eta = \left(\frac{C_0 - C}{C_0}\right) \times 100$$

where C_0 is the initial concentration of the dye or phenol in the solution, and C is the final concentration after the light exposure and catalyst removal in the solution. The synthesized CeO_2 and U-CeO_{2-x} showed BB degradation rates of about 44% and 95.2%, respectively, after 30 min of irradiation, while 39% and 94.5% phenol degradation rates
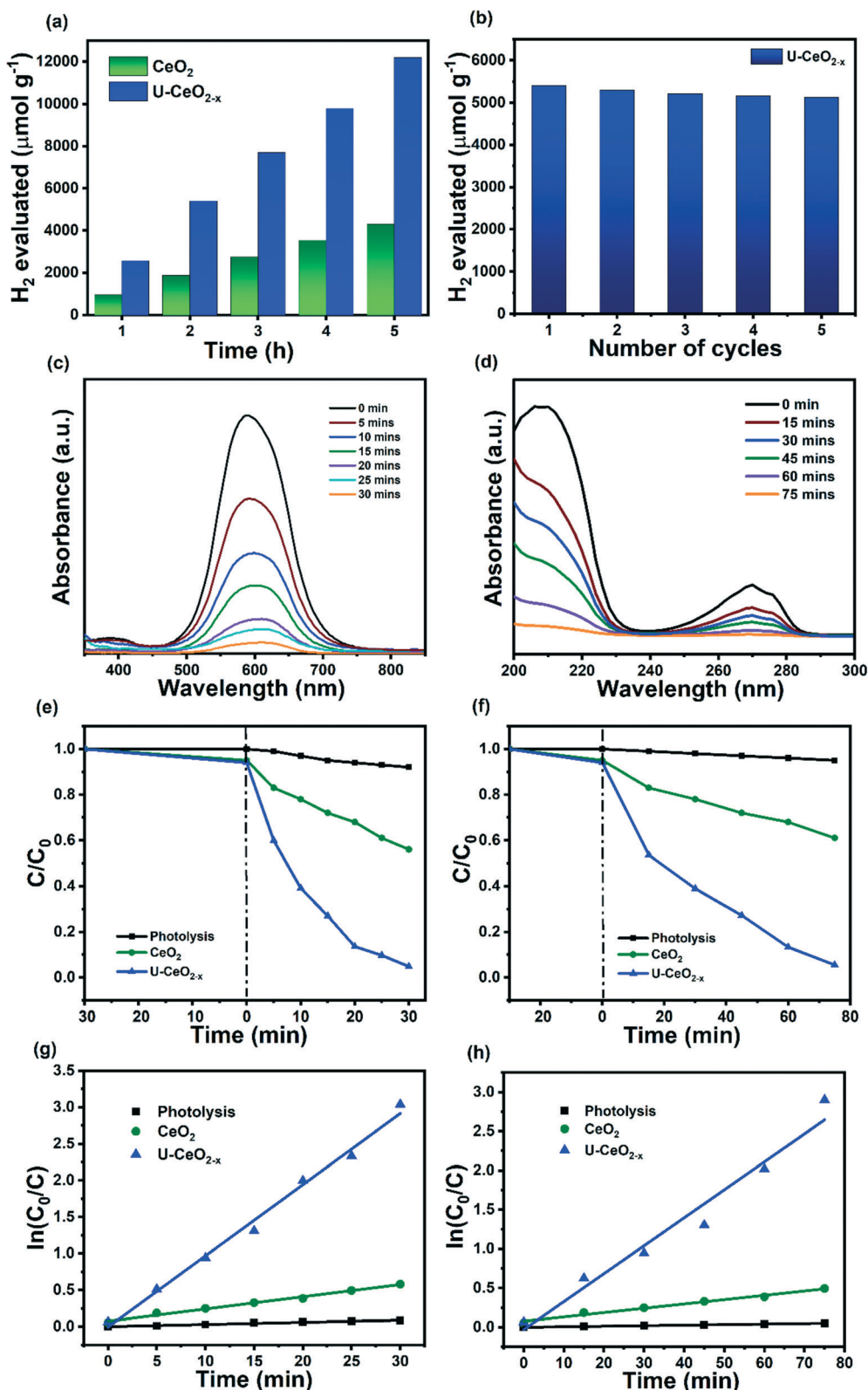
This journal is © The Royal Society of Chemistry 2022

Catal. Sci. Technol., 2022, **12**, 2071–2083 | **2077**

Fig. 4 (a) Photocatalytic H_2 production rate of CeO_2 and $U\text{-}CeO_{2-x}$; (b) reproducibility of H_2 production of $U\text{-}CeO_{2-x}$; photodegradation curves of (c) BB dye and (d) phenol for different time intervals over $U\text{-}CeO_{2-x}$; adsorption and photocatalytic activity on (e) BB dye and (f) phenol; degradation kinetics of (g) BB dye and (h) phenol over the synthesized samples.

for CeO_2 and $U\text{-}CeO_{2-x}$, respectively, were observed after 75 min of irradiation. The study clearly shows that the

degradation follows pseudo-first-order kinetics,[54] which is given as,

Table 1 Comparison of the H_2 production of the CeO_2-based catalysts

Catalyst	Synthesis method	Light source	H_2 production (in μmol for 5 h)	Reference
U-CeO_{2-x}	Ultrasound treatment	300 W Xe lamp $\geq$420 nm	12 850	This work
$rCeO_2$/g-C_3N_4	Self-assembly	300 W Xe lamp $\geq$420 nm	5500	16
CeO_2/gC_3N_4-5%	Self-assembly	300 W Xe lamp $\geq$420 nm	4300	3
1.5%CeO_2/g-C_3N_4	Facial synthesis	300 W Xe lamp $\geq$420 nm	4150	47
CeO_2@N,S–C HN	Calcination	300 W Xe lamp $\geq$420 nm	2775	48
15%$W_{18}O_{49}$/CeO_2	Hydrothermal	300 W Xe lamp $\geq$420 nm	1030	49
$Mn_{0.2}Cd_{0.8}S$/CeO_2	Solvothermal	5 W Xe lamp $\geq$400 nm	655	50
1T/2H-MoS_2@CeO_2	Hydrothermal	3 W UV-LEDs $\geq$420 nm	366	51
CeO_2@MoS_2/gC_3N_4	Hydrothermal	3 W UV-LEDs $\geq$420 nm	327	52
CeO_2/ZnO	Electrodeposition	300 W Xe lamp $\geq$420 nm	13.5	53

$$\ln(C_0/C) = kt$$

where k denotes the rate constant of the pseudo-first-order reaction while C and C_0 are the dye concentration in the suspension at time t and t_0, respectively. Fig. 4g shows the pseudo-first-order kinetic studies of the BB degradation displaying the rate constants of 0.017 and 0.097 min^{-1} for CeO_2 and U-CeO_{2-x}, respectively, whereas the rate constant of 0.005 and 0.036 min^{-1} was observed for phenol degradation under CeO_2 and U-CeO_{2-x}, respectively, as shown in Fig. 4h.

Total organic carbon was measured to get the degree of the mineralization and it was found that phenol was mineralized better than BB dye (see Fig. S3†). TOC results were found to mineralize about 50% in 30 min and 61% in 80 min for BB dye and phenol, respectively.

The data obtained by several researchers as reported in Table S2† show that phenol has longer degradation time than brilliant blue dye. This is mainly due to brilliant blue dye being a photosensitizer that absorbs more light so the photoreaction takes place rapidly. Moreover, the degradation pathway of BB dye (see Fig. S6†) shows the disappearance of the reactant and breaking into two different compounds within 30 min implying that it wasn't completely mineralized. According to the conventional spectrophotometric method, the lambda max of BB dye almost disappeared within 30 min.

3.3. Photocatalytic mechanism

In order to explore the mechanism behind U-CeO_{2-x} 's excellent photocatalytic H_2 production and water treatment, the band locations of CeO_2 and U-CeO_{2-x} were identified using the Tauc plot derived from the UV-DRS spectra. By utilizing the band gaps of the samples, the corresponding

VBM and CBM values were calculated using the following equations:

$$VBM = \chi - E_H + \frac{E_g}{2}$$

$$CBM = VBM - E_g$$

where E_H = 4.5 eV represents the energy of free electrons on a hydrogen scale, χ = 5.56 eV is the electronegativity of CeO_2, and E_g is the band gap. The calculated values of VBM and CBM were found to be 2.7 and −0.58 eV for CeO_2, along with 2.63 and −0.51 eV for U-CeO_{2-x}, respectively.

The degradation mechanism was simulated in the presence of scavengers under optimal conditions in order to establish the most reactive species, namely, p-benzoquinone (BQ), sodium azide (NaN_3), and isopropanol (IPA) for superoxide radicals ($^{\cdot}O_2^-$), singlet oxygen ($^1O_2$), and hydroxyl radicals ($^{\cdot}OH$), respectively. The addition of BQ into the reaction system displayed less efficiency illustrating the influence of $^{\cdot}O_2^-$. The presence of NaN_3 quenched the reaction to a larger extent with the least efficiency exhibiting the impact of surface oxygen vacancies.[55] In comparison, the addition of the IPA scavenger showed a better photodegradation efficiency indicating the lower contribution of $^{\cdot}OH$ radicals in the pollutant removal. Thus, the scavenger test illustrates the significant involvement of $^{\cdot}O_2^-$, $^1O_2$, and $^{\cdot}OH$ in the degradation process as shown in Fig. 5a. ESR analysis was performed to confirms the presence of the above ROS by employing radical trapping substances. The generated $^{\cdot}OH$ was detected by using DMPO as a radical trapping substance in an aqueous solution.[8] Fig. S4† shows the ESR signal for the CeO_{2-x} sample in the dark and under solar simulated light. Under dark conditions, no amount of
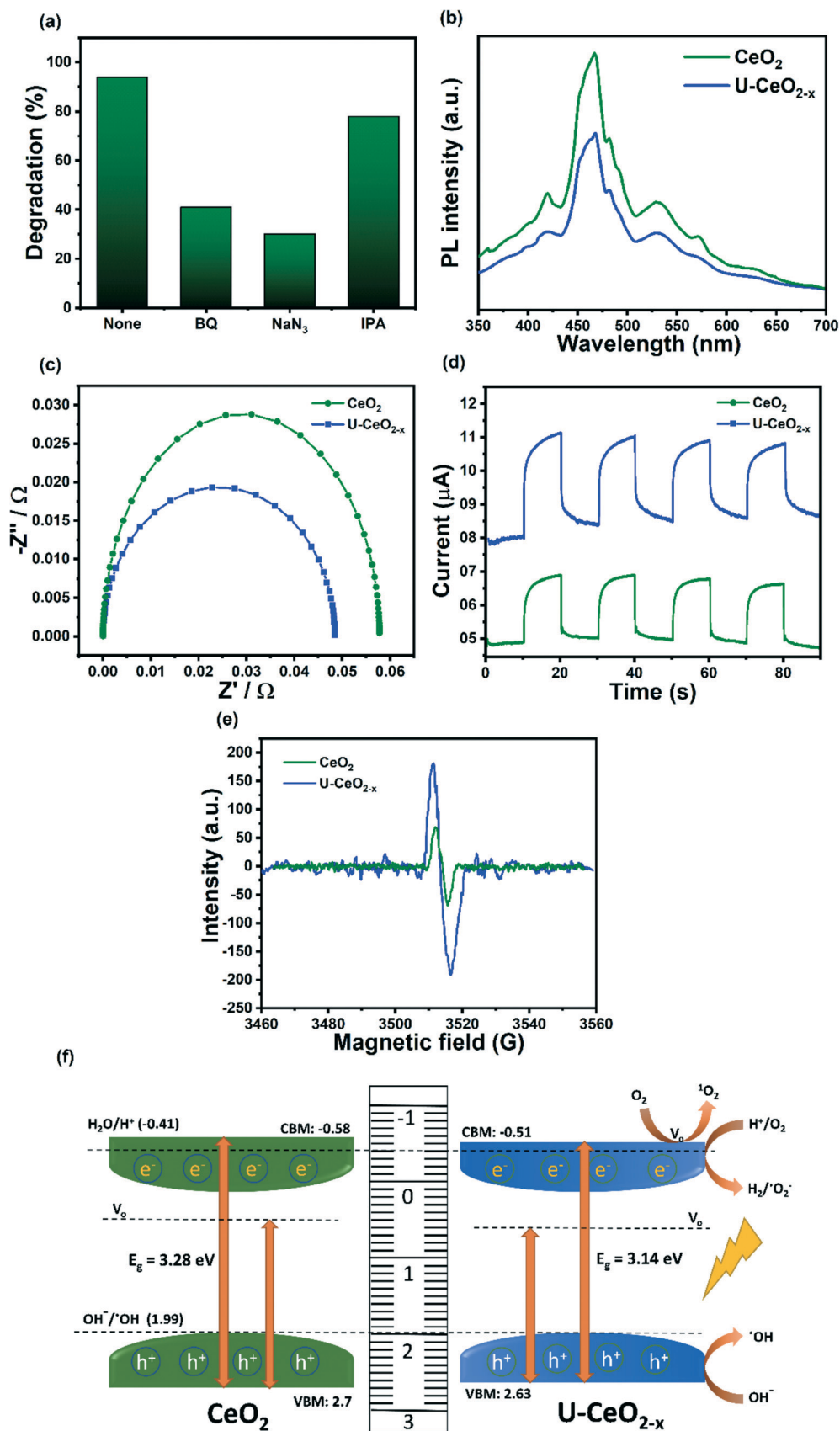
Fig. 5 (a) Scavenger's test for photodegradation, (b) photoluminescence spectra, (c) electrochemical impedance spectroscopy results, (d) photocurrent response, and (e) ESR spectra of the prepared samples; (f) energy band positions of CeO_2 and $U-CeO_{2-x}$.

2080 | *Catal. Sci. Technol.*, 2022, **12**, 2071–2083

This journal is © The Royal Society of Chemistry 2022

˙OH was detected; however, the characteristic peaks of DMPO–˙OH appeared while irradiated, suggesting the generation of ˙OH. The ˙O$_2^-$ was identified using DMPO in the methanol solution and no distinctive peaks were observed in the dark, while the characteristic DMPO–˙O$_2^-$ peaks were observed as shown in Fig. S5.† The ^{1}O$_2$ generation was confirmed by employing TEMP as a trapping substance.[54] Fig. S6† shows no peaks under dark conditions and a distinctive TEMPO peak when illuminated, confirming the presence of ^{1}O$_2$.

The charge recombination rate and the electronic structure of the synthesized samples were studied by PL measurements. The PL spectra of CeO$_2$ and U-CeO$_{2-x}$ recorded in the range of 350 nm to 700 nm with a 410 nm excitation wavelength are shown in Fig. 5b. A fine UV emission band around 359.4 nm originates due to the near bandgap emission of CeO$_2$. A visible emission peak at 419.8 nm arises in the violet region, while significant peaks in the spectra at 467.2 and 481.4 nm emerge in the blue region. Besides, a strong green emission peak at 529.9 nm and a trifling peak at 572.16 nm are observed.[56] Altogether, the visible emission bands correspond to oxygen vacancies by the transfer of charge carriers.[57] The decrease in the intensity of the U-CeO$_{2-x}$ peaks is due to having a higher content of oxygen vacancies, which allows the excited states to have an extended lifetime. Thus, the PL spectra show efficient charge separation of U-CeO$_{2-x}$ for higher photocatalytic activity.
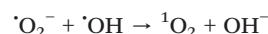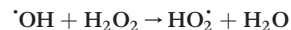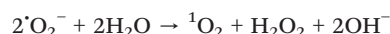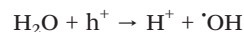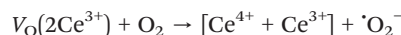
The impedance Nyquist plots were obtained to confirm the electron–hole separation efficiency of the ceria samples, as shown in Fig. 5c. The intended response of a simple circuit is shown by the semicircle arc in the Nyquist plot, which explains the charge transfer resistance. The contributions from the charge transfer resistance (R_{ct}) and constant phase element from the sample's interface are ascribed to the semicircular arcs in the EIS spectra.[58] A substantial shift in the R_{ct} value is observed due to the formation of surface defects on the U-CeO$_{2-x}$ nanostructure.[59] Accordingly, the semicircle radius of U-CeO$_{2-x}$ in the EIS is smaller, indicating a lower resistance and effective separation of photogenerated electron–hole pairs and faster interfacial charge transfer. Thus, EIS evidences that the surface defect-induced U-CeO$_{2-x}$ sample has higher charge carrier separation efficiency and better photocatalytic activity.

Fig. 5d shows the photocurrent densities of the CeO$_2$ and U-CeO$_{2-x}$ samples, which were measured in the dark and under visible light irradiation to examine the photoreactivity. The improvement in the photocurrent response of U-CeO$_{2-x}$ is attributed to an increase in light absorption capacity caused by surface defects that generate a mid-gap state, which assists in narrowing the bandgap.[60] In general, a high photocurrent indicates that the sample possesses a significant capacity to generate and transmit the photoexcited charge carrier when exposed to light radiation. The photocurrent of U-CeO$_{2-x}$ is greater than those of its counterpart under the same parameters, indicating that U-CeO$_{2-x}$ has a better capacity in the separation of electron–

hole pairs. Thus, the enhanced photocatalytic activity of the U-CeO$_{2-x}$ sample can be attributed to the excellent light-harvesting capacity and the efficient separation of photogenerated charge carriers.

The ESR signals were studied to probe the oxidation states of the ceria samples, and Fig. 5e shows the ESR spectra of the CeO$_2$ and U-CeO$_{2-x}$ samples. The ESR spectra of the samples were recorded at room temperature under a 100 kHz modular frequency. A strong signal is observed at g = 1.96 and mainly attributed to Ce^{3+} ions in the synthesized samples.[60] The U-CeO$_{2-x}$ sample shows an increased intensity signal, owing to the reduction of Ce^{4+} to Ce^{3+} ions. These Ce^{3+} ion's trigonal sites are recognized as near-surface oxygen defects.[61] Accordingly, the two samples show a single ESR signal corresponding to oxygen vacancies, and the signal intensity is very high for the U-CeO$_{2-x}$ sample. Thus, the U-CeO$_{2-x}$ sample showed the presence of Ce^{3+} ions and a higher concentration of oxygen vacancies.

Based on the position of the VBM and CBM of the samples, the band energy alignment and the photocatalytic mechanism are shown in Fig. 5f. When the sample is exposed to visible light irradiation, electron and hole pairs are generated. The photogenerated electrons accumulated on the CBM with a reduction potential higher than H$^+$/H$_2$ resulting in photocatalytic H$_2$ production.[17] The U-CeO$_{2-x}$ sample was comprised of Ce^{3+} and oxygen vacancies on the surface layer assisting the H$_2$ production pathway. On the other hand, when Ce^{4+} oxidizes to Ce^{3+}, oxygen vacancies (V_O) may develop on the surface of CeO$_2$ and O$_2$ gets adsorbed on the surface to produce ˙O$_2^-$.[28] Similar to the Haber–Weiss reaction, the self-combination of ˙O$_2^-$ leads to the generation of ^{1}O$_2$. Besides, the generated ˙OH reacts with ˙O$_2^-$ to produce ^{1}O$_2$ signifying its major role in degrading pollutants.[62] The three reactive oxygen species (ROS), ˙O$_2^-$, ^{1}O$_2$, and ˙OH, reduce the organic pollutants into intermediates leading to the decomposition.

$$V_O(2Ce^{3+}) + O_2 \rightarrow [Ce^{4+} + Ce^{3+}] + \cdot O_2^-$$

$$H_2O + h^+ \rightarrow H^+ + \cdot OH$$

$$2\cdot O_2^- + 2H_2O \rightarrow {}^1O_2 + H_2O_2 + 2OH^-$$

$$\cdot OH + H_2O_2 \rightarrow HO_2^{\cdot} + H_2O$$

$$HO_2^{\cdot} \rightarrow H + \cdot O_2^-$$

$$\cdot O_2^- + \cdot OH \rightarrow {}^1O_2 + OH^-$$

$$^1O_2 + \text{pollutants} \rightarrow \text{Intermediate products}$$

The intermediate compounds produced during the degradation process were identified by LC-MS at different

time intervals. Based on the obtained LC-MS results shown in Fig. S6,† the degradation pathway of BB was proposed and illustrated in Fig. S7.† Some of the compounds mentioned in the degradation pathway were not identified by LC-MS analysis (such as $m/z = 240$, $m/z = 218.06$, $m/z = 166.22$, and $m/z = 106.16$). Those compounds were reported previously.[63,64] Noticeably, the smallest compound identified by LC-MS spectroscopy was with $m/z = 122.17$ indicating that the mineralization was not complete within 30 min. Similarly, the phenol degradation intermediates were identified by LC-MS analysis and are shown in Fig. S8.† A plausible phenol degradation route was suggested as shown in Fig. S9.† The mechanism of phenol oxidative mineralization begins with the formation of toxic quinones, followed by the opening of the aromatic ring, which results in the formation of biodegradable aliphatic acids and eventually, mineralization of the phenol to carbon dioxide and water. A similar degradation pathway was reported earlier.[65]

When the ceria solution is subjected to low ultrasonic irradiation, bubbles are formed and squashed by the solution's sonic field. This acoustic cavitation effect leads to a larger surface area, high crystallinity, relatively smaller particle size and phase purity of the sample.[66] Furthermore, the ultrasound treatment energizes the chemical reactions in the liquids by producing significant collisions and shock waves, which contribute to particle aggregation and surface defects leading to oxygen vacancy formation.[24] Thus, the ultrasound treatment enhances photocatalytic hydrogen evolution and pollutant degradation.

4. Conclusion

Defect engineering of the ceria nanoparticles with oxygen vacancies was achieved for the first time using low-frequency ultrasound treatment. The U-CeO$_{2-x}$ sample showed high crystallinity, and morphological changes were observed. Due to the acoustic cavitation effect, a larger surface area and small particle size were observed. The ultrasound treatment causes particle aggregation and surface defects leading to oxygen vacancy formation. The XPS, Raman spectroscopy, PL spectroscopy and ESR results confirm the presence of oxygen vacancies. The ultrasound-treated sample was also examined for pollutant degradation, where $^1O_2$ was found to be the major active species. Hence, the ultrasound treatment influences efficient photocatalysts for superior hydrogen evolution and an excellent photocatalytic degradation of contaminants. The prepared nanostructure showed excellent stability and recyclability. This work could pave the way for a unique post-synthesis strategy intended for efficient photocatalytic nanostructures.

Conflicts of interest

There are no conflicts to declare.

Acknowledgements

References

1 D. Bahnemann, *Sol. Energy*, 2004, **77**, 445–459.

2 M. Balat, *Int. J. Hydrogen Energy*, 2008, **33**, 4013–4029.

3 W. Zou, Y. Shao, Y. Pu, Y. Luo, J. Sun, K. Ma, C. Tang, F. Gao and L. Dong, *Appl. Catal., B*, 2017, **218**, 51–59.

4 S. Ahmed, M. Rasul, W. N. Martens, R. Brown and M. Hashib, *Water, Air, Soil Pollut.*, 2011, **215**, 3–29.

5 H. T. Bui, S. Weon, J. W. Bae, E.-J. Kim, B. Kim, Y.-Y. Ahn, K. Kim, H. Lee and W. Kim, *J. Hazard. Mater.*, 2021, **404**, 123976.

6 M. Wang, M. Shen, X. Jin, J. Tian, M. Li, Y. Zhou, L. Zhang, Y. Li and J. Shi, *ACS Catal.*, 2019, **9**, 4573–4581.

7 A. Hezam, K. Namratha, Q. A. Drmosh, D. Ponnamma, J. Wang, S. Prasad, M. Ahamed, C. Cheng and K. Byrappa, *ACS Appl. Nano Mater.*, 2019, **3**, 138–148.

8 K. Alkanad, A. Hezam, Q. A. Drmosh, G. C. Sujay Shekar, A. A. AlObaid, I. Warad, M. A. Bajiri and L. Neratur Krishnappagowda, *Sol. RRL*, 2021, 2100501.

9 R. Shi, Y. Zhao, G. I. Waterhouse, S. Zhang and T. Zhang, *ACS Catal.*, 2019, **9**, 9739–9750.

10 S. Bai, N. Zhang, C. Gao and Y. Xiong, *Nano Energy*, 2018, **53**, 296–336.

11 J. Holgado, G. Munuera, J. Espinós and A. González-Elipe, *Appl. Surf. Sci.*, 2000, **158**, 164–171.

12 H. Zhao, F. Pan and Y. Li, *J. Materiomics*, 2017, **3**, 17–32.

13 S. N. Naidi, F. Khan, A. L. Tan, M. H. Harunsani, Y.-M. Kim and M. M. Khan, *New J. Chem.*, 2021, **45**, 7816–7829.

14 M. M. Khan, S. A. Ansari, D. Pradhan, D. H. Han, J. Lee and M. H. Cho, *Ind. Eng. Chem. Res.*, 2014, **53**, 9754–9763.

15 S. N. Naidi, M. H. Harunsani, A. L. Tan and M. M. Khan, *J. Mater. Chem. B*, 2021, **9**, 5599–5620.

16 W. Zou, B. Deng, X. Hu, Y. Zhou, Y. Pu, S. Yu, K. Ma, J. Sun, H. Wan and L. Dong, *Appl. Catal., B*, 2018, **238**, 111–118.

17 B. Chen, Y. Ma, L. Ding, L. Xu, Z. Wu, Q. Yuan and W. Huang, *J. Phys. Chem. C*, 2013, **117**, 5800–5810.

18 B. Choudhury and A. Choudhury, *Mater. Chem. Phys.*, 2012, **131**, 666–671.

19 L. Zhang, Q. Fang, Y. Huang, K. Xu, P. K. Chu and F. Ma, *Anal. Chem.*, 2018, **90**, 9821–9829.

20 J. Vecchietti, P. Lustemberg, E. L. Fornero, M. Calatayud, S. E. Collins, S. Mohr, M. V. Ganduglia-Pirovano, J. Libuda and A. L. Bonivardi, *Appl. Catal., B*, 2020, **277**, 119103.

21 S. N. Naidi, F. Khan, A. L. Tan, M. H. Harunsani, Y.-M. Kim and M. M. Khan, *Biomater. Sci.*, 2021, **9**, 4854–4869.

22 H. Dong, G. Zeng, L. Tang, C. Fan, C. Zhang, X. He and Y. He, *Water Res.*, 2015, **79**, 128–146.

2082 | *Catal. Sci. Technol.*, 2022, **12**, 2071–2083

This journal is © The Royal Society of Chemistry 2022

23 B. E. Noltingk and E. A. Neppiras, *Proc. Phys. Soc., London, Sect. B*, 1950, **63**, 674.

24 N. Zhang, G. Zhang, S. Chong, H. Zhao, T. Huang and J. Zhu, *J. Environ. Manage.*, 2018, **205**, 134–141.

25 A. Bayrami, E. Ghorbani, S. R. Pouran, A. Habibi-Yangjeh, A. Khataee and M. Bayrami, *Ultrason. Sonochem.*, 2019, **58**, 104613.

26 M. Ruiz-Hernando, J. Labanda and J. Llorens, *Biochem. Eng. J.*, 2010, **52**, 131–136.

27 K. Kaviyarasu, P. Murmu, J. Kennedy, F. Thema, D. Letsholathebe, L. Kotsedi and M. Maaza, *Nucl. Instrum. Methods Phys. Res., Sect. B*, 2017, **409**, 147–152.

28 G. C. Sujay Shekar, K. Alkanad, A. Hezam, A. Alsalme, N. Al-Zaqri and N. Lokanath, *J. Mol. Liq.*, 2021, **335**, 116186.

29 R. Bakkiyaraj, G. Bharath, K. H. Ramsait, A. Abdel-Wahab, E. H. Alsharaeh, S.-M. Chen and M. Balakrishnan, *RSC Adv.*, 2016, **6**, 51238–51245.

30 L. R. Yadav, K. Manjunath, B. Archana, C. Madhu, H. R. Naika, H. Nagabhushana, C. Kavitha and G. Nagaraju, *Eur. Phys. J. Plus*, 2016, **131**, 1–10.

31 E. Bêche, P. Charvin, D. Perarnau, S. Abanades and G. Flamant, *Surf. Interface Anal.*, 2008, **40**, 264–267.

32 Y. Wang, Y. Wu, H. Yang, M. Wang, X. Shi, C. Wang and S. Zhang, *Mater. Technol.*, 2018, **33**, 48–56.

33 A. Hezam, J. Wang, Q. Drmosh, P. Karthik, M. A. Bajiri, K. Namratha, M. Zare, T. Lakshmeesha, S. Shivanna and C. Cheng, *Appl. Surf. Sci.*, 2021, **541**, 148457.

34 C. Ma, J. Fu, J. Chen, Y. Wen, P. O. Fasan, H. Zhang, N. Zhang, J. Zheng and B.-H. Chen, *Ind. Eng. Chem. Res.*, 2017, **56**, 9090–9097.

35 J. Li, R. Hu, J. Zhang, W. Meng, Y. Du, Y. Si and Z. Zhang, *Fuel*, 2016, **178**, 148–154.

36 L. Xue, C. Zhang, H. He and Y. Teraoka, *Appl. Catal., B*, 2007, **75**, 167–174.

37 Y. Sun, Y. Gao, C. He, W. Song, Z. Jiang, R. Albilali and B. Bai, *Catal. Sci. Technol.*, 2021, **11**, 3762–3774.

38 Z. Ma, S. Zhao, X. Pei, X. Xiong and B. Hu, *Catal. Sci. Technol.*, 2017, **7**, 191–199.

39 B. Wang, B. Chen, Y. Sun, H. Xiao, X. Xu, M. Fu, J. Wu, L. Chen and D. Ye, *Appl. Catal., B*, 2018, **238**, 328–338.

40 A. A. Kokhanovsky, *J. Phys. D: Appl. Phys.*, 2007, **40**, 2210.

41 P. Patsalas, S. Logothetidis, L. Sygellou and S. Kennou, *Phys. Rev. B: Condens. Matter Mater. Phys.*, 2003, **68**, 035104.

42 H. Ebendorff-Heidepriem and D. Ehrt, *Opt. Mater.*, 2000, **15**, 7–25.

43 T. Ramanathan, S. Stankovich, D. Dikin, H. Liu, H. Shen, S. Nguyen and L. Brinson, *J. Polym. Sci., Part B: Polym. Phys.*, 2007, **45**, 2097–2112.

44 L. Wang, H. Ji, S. Wang, L. Kong, X. Jiang and G. Yang, *Nanoscale*, 2013, **5**, 3793–3799.

45 E. Poonia, P. K. Mishra, V. Kiran, J. Sangwan, R. Kumar, P. K. Rai, R. Malik, V. K. Tomer, R. Ahuja and Y. K. Mishra, *J. Mater. Chem. C*, 2019, **7**, 5477–5487.

46 M. Aslam, M. Qamar, M. T. Soomro, I. M. Ismail, N. Salah, T. Almeelbi, M. Gondal and A. Hameed, *Appl. Catal., B*, 2016, **180**, 391–402.

47 X. Liu, L. He, X. Chen, L. Du, X. Gu, S. Wang, M. Fu, F. Dong and H. Huang, *Int. J. Hydrogen Energy*, 2019, **44**, 16154–16163.

48 J. Hao, W. Zhan, L. Sun, G. Zhuang, X. Wang and X. Han, *Inorg. Chem.*, 2019, **59**, 937–942.

49 C. H. Shen, X. J. Wen, Z. H. Fei, Z. T. Liu and Q.-M. Mu, *J. Colloid Interface Sci.*, 2020, **579**, 297–306.

50 Y. Wang, X. Hao, L. Zhang, Y. Li and Z. Jin, *Energy Fuels*, 2020, **34**, 2599–2611.

51 C. Zhu, Q. Xian, Q. He, C. Chen, W. Zou, C. Sun, S. Wang and X. Duan, *ACS Appl. Mater. Interfaces*, 2021, **13**, 35818–35827.

52 C. Zhu, Y. Wang, Z. Jiang, F. Xu, Q. Xian, C. Sun, Q. Tong, W. Zou, X. Duan and S. Wang, *Appl. Catal., B*, 2019, **259**, 118072.

53 C.-H. Zeng, S. Xie, M. Yu, Y. Yang, X. Lu and Y. Tong, *J. Power Sources*, 2014, **247**, 545–550.

54 K. Alkanad, A. Hezam, G. C. Sujay Shekar, Q. Drmosh, A. A. Kala, M. Q. AL-Gunaid and N. Lokanath, *Catal. Sci. Technol.*, 2021, **11**, 3084–3097.

55 J. Zhao, F. Li, H. Wei, H. Ai, L. Gu, J. Chen, L. Zhang, M. Chi and J. Zhai, *Chem. Eng. J.*, 2021, **409**, 128150.

56 S. Kumar, A. K. Ojha, D. Patrice, B. S. Yadav and A. Materny, *Phys. Chem. Chem. Phys.*, 2016, **18**, 11157–11167.

57 B. Choudhury, P. Chetri and A. Choudhury, *J. Exp. Nanosci.*, 2015, **10**, 103–114.

58 A. Hezam, K. Namratha, D. Ponnamma, Q. Drmosh, A. M. N. Saeed, C. Cheng and K. Byrappa, *ACS Omega*, 2018, **3**, 12260–12269.

59 S. A. Ansari, M. M. Khan, M. O. Ansari, S. Kalathil, J. Lee and M. H. Cho, *RSC Adv.*, 2014, **4**, 16782–16791.

60 M. E. Khan, M. M. Khan and M. H. Cho, *Sci. Rep.*, 2017, **7**, 1–17.

61 Z.-Q. Wang, M.-J. Zhang, X.-B. Hu, V. P. Dravid, Z.-N. Xu and G.-C. Guo, *Chem. Commun.*, 2020, **56**, 403–406.

62 Z. Li, D. Liu, Y. Zhao, S. Li, X. Wei, F. Meng, W. Huang and Z. Lei, *Chemosphere*, 2019, **233**, 549–558.

63 M. Saquib and M. Muneer, *Dyes Pigm.*, 2002, **53**, 237–249.

64 M. P. Rayaroth, U. K. Aravind and C. T. Aravindakumar, *Chemosphere*, 2015, **119**, 848–855.

65 T. T. T. Dang, S. Le, D. Channei, W. Khanitchaidecha and A. Nakaruk, *Res. Chem. Intermed.*, 2016, **42**, 5961–5974.

66 M. Ashokkumar, *Ultrason. Sonochem.*, 2011, **18**, 864–872.

This journal is © The Royal Society of Chemistry 2022

Catal. Sci. Technol., 2022, **12**, 2071–2083 | **2083**